Tri-Directional Sub-Voxel Displacement and Ipsilateral Territory Decoupling for 3D Bilateral Coronary Artery Tree Reconstruction in Cardiac CT Angiography

Zeyu Jia and Xin Ming

arXiv:2610.05900v2 [cs.CV] 27 Oct 2026

Abstract—Three-dimensional (3D) reconstruction of bilateral coronary trees (LCA and RCA) from cardiac computed tomography angiography (CCTA) is limited by 64^3 quantization, territory ambiguity, and sinotubular junction (STJ) ostium drift. We present a canonical $SO(3)$ $(Z_{\text{IS}}, Y_{\text{PA}}, X_{\text{LR}})$ multi-scale representation and Riemannian arborescence framework. First, we map 3D CCTA volumes, centerlines, and thick-stem ostia into $(Z_{\text{IS}}, Y_{\text{PA}}, X_{\text{LR}})$ space, extending a 3D pyramid and tubular decoder with a $128^3 \to 64^3$ boundary skip, a stop-gradient 128^3 residual branch, a sub-voxel displacement head $\Delta\hat{\mathbf{u}}(\mathbf{x})$, a dual-channel ipsilateral head $(\mathbf{P}_{\text{LCA}}, \mathbf{P}_{\text{RCA}})$, and a 32^3 ostium detector. Second, all $327,385$ active parameters ($398,843$ total) are trained in one 30-epoch AdamW loop ($\epsilon = 10^{-8}$) under decoupled L2-SP and aortic-wall consistency. Third, our Riemannian solver couples cylindrical Valsalva-STJ calibration, 128^3 orifice contact rooting, contralateral inhibition, centripetal pruning, and 4-stage curvature-adaptive normal-plane pullback. On 14 unseen ImageCAS development volumes (28 trees; cases 201–250 isolated), the framework achieves 2.1652 ± 0.4686 mm CD_{CL} ($\text{CD}_{\text{CL}}^{\text{arc1mm}} = 2.2697 \pm 0.4863$ mm, $p \leq 0.00024$; $57.40\%/78.20\%$ F1@1/2mm; $4.6880/4.9298$ mm ostia). Zero-shot evaluation on 50 unseen volumes (Cases 251–300, 100 trees) yields 2.9389 ± 1.2785 mm CD_{CL} ($p \leq 7.24 \times 10^{-7}$; ostia $5.1815/7.5442$ mm), with 2.7696 ± 1.1919 mm pooled $N = 64$ CD_{CL} and $128/128$ trees ($\beta_0 = 1, \beta_1 = 0$, 0.0000 mm detachment).

Index Terms—Coronary CT Angiography, 3D Vascular Tree Reconstruction, Sub-Voxel Displacement Field, Ipsilateral Territory Decoupling, Riemannian Minimal Arborescence, Murray's Law, L2-SP Regularization.

1 Introduction

ACCURATE three-dimensional (3D) reconstruction of bilateral coronary arterial trees—comprising the left coronary artery (LCA, branching into the left anterior descending and circumflex territories) and the right coronary artery (RCA)—from cardiac computed tomography angiography (CCTA) is a foundational prerequisite for anatomical quantitative assessment and computational hemodynamic simulation [1]–[4]. As demonstrated in recent topology-focused benchmarks [5]–[7], high voxel-wise segmentation overlap (Dice) does not ensure anatomical tree continuity or prevent cross-territory structural errors: a dense 3D segmentation network may sever thin distal vessels ($r < 1.0$ mm) due to partial-volume contrast attenuation or erroneously fuse adjacent LCA and RCA branches in the posterior atrioventricular groove.

Within coarse-to-fine 3D vascular tree generation pipelines [8]–[10], diagnostic analysis on the ImageCAS benchmark [4] reveals three primary bottlenecks limiting centerline precision on 64^3 feature lattices:

1) **Nyquist Discretization Floor on 64^3 Grids**: Decoding a 128^3 CCTA crop spanning 160–200 mm onto a 64^3 lattice (voxel spacing $\sim$ 2.5–3.1 mm) incurs a quantization offset of 0.8–1.2 mm, causing unrefined sub-millimeter precision (F1@1mm) to stagnate near 12%.
2) **Single-Channel Territory Ambiguity and Axis Alignment**: A scalar probability field $\mathbf{P}_{\text{lumen}}(\mathbf{x}) \in [0,1]^{64^3}$ cannot separate adjacent LCA and RCA branches. Moreover, raw NIfTI arrays in Fortran order $(X_{\text{RL}}, Y_{\text{PA}}, Z_{\text{IS}})$ must be mapped via $\mathcal{T}_{\text{can}} \in SO(3)$ ($\det = +1$) to canonical $(Z_{\text{IS}}, Y_{\text{PA}}, X_{\text{LR}})$ space while preserving full-topology LCA/RCA partitions and connected thick-stem aortic-wall ostium landmarks.
3) **Recall-Preserving Joint Optimization vs. Representation Drift**: Unregularized fine-tuning can erode vessel recall or inflate background drift. Jointly optimizing all active parameters with decoupled L2-SP anchoring and contrast-sharpening constraints preserves tubular signal-to-noise ratio (validation SNR $= 8.34\times$, median centerline probability 0.5810 vs. far-field 95th-percentile background 0.0696).

To address these coupled challenges, we present a unified 3D bilateral coronary arborescence framework in canonical $SO(3)$ $(Z_{\text{IS}}, Y_{\text{PA}}, X_{\text{LR}})$ space (Fig. 1) with four technical contributions:

1) $128^3 \to 64^3$ **Boundary Skip, Native 128^3 Residual Tubular Decoder, and Continuous 3D Sub-Voxel Displacement Field**: We extend the 3D tubular segmentation decoder with a stride-2 boundary skip ($\mathbf{H}_{128}$), a native 128^3 residual branch predicting $\mathbf{P}_{\text{lumen},128}(\mathbf{x}) \in [0,1]^{128^3}$ under stop-gradient backbone isolation, and a zero-initialized 3D sub-

Zeyu Jia is with the School of Biomedical Engineering and Technology, Tianjin Medical University, Tianjin 300070, China, and also with the Medical School, Tianjin University, Tianjin 300072, China (e-mail: jiazeyu@tju.edu.cn). Xin Ming is with the School of Biomedical Engineering and Technology, Tianjin Medical University, Tianjin 300070, China. Corresponding author: Xin Ming.

voxel displacement head predicting $\Delta\hat{\mathbf{u}}(\mathbf{x}) \in [-2.0, +2.0]^3$ mm.

2) **Dual-Channel Ostium-Conditioned Ipsilateral Decoupling**: A residual dual-channel ipsilateral head combines multi-scale 3D features with canonical coordinates $\mathbf{G}_{64} \in [0,1]^3$ to predict $\hat{A}_{\text{ipsi}}(\mathbf{x} \mid \mathbf{r}_s) = (\mathbf{P}_{\text{LCA}}(\mathbf{x}), \mathbf{P}_{\text{RCA}}(\mathbf{x}))$ under contralateral hard-negative suppression.
3) **Single-Loop Recall-Preserving Canonical $SO(3)$ Multi-Task Optimization**: We standardize all volumes, centerlines, and thick-stem ostia via $\mathcal{T}_{\text{can}} \in SO(3)$ (axis permutation $(X, Y, Z) \mapsto (Z, Y, X)$ followed by right-to-left sagittal reflection, $\det = +1$), initialize from the recall-balanced canonical reference checkpoint, and train all $327,385$ active parameters ($81,008$ in the 3D pyramid encoder, $121,183$ in the tubular decoder, and $125,194$ in the 3D ostium landmark detector, out of $398,843$ total parameters) in a single 30-epoch AdamW loop ($\epsilon = 10^{-8}$) with decoupled L2-SP and per-step EMA anchoring ($\gamma_{\text{sp}} = 0.06$ on the final 1^3 projection layer and $\gamma_{\text{sp}} = 0.75$ on remaining base encoder/lumen and 64^3 multi-task layers).
4) **Riemannian Geodesic Arborescence with Cylindrical Sinus-Wall Calibration, Native-128^3 Orifice Contact Rooting, and Curvature-Adaptive Pullback**: Within our Riemannian geodesic arborescence solver, we couple coordinate-free cylindrical Valsalva-STJ wall calibration ($[-16.0, +18.0]$ mm), conservative cylindrical sinus-wall rooting with geodesic inflow stems, Stage-M_3 native-128^3 Valsalva-orifice contact expectation, Stage-M_4 native 128^3 residual coupling, pure contralateral inhibition, a centripetal survival functional, and curvature-adaptive normal-plane pullback $(\mathbf{I} - \mathbf{T}\mathbf{T}^\top)\Delta\hat{\mathbf{u}}(\mathbf{x})$ preserving $\beta_0 = 1$, $\beta_1 = 0$ and 0.0000 mm root detachment.

2 Related Work

2.1 3D Coronary Artery Segmentation and Centerline Extraction

Deep learning methods for 3D coronary tree extraction follow either dense voxel segmentation followed by skeletonization [4], [5], [11]–[13] or explicit centerline graph/trajectory modeling [7]–[10], [14], [15]. While clDice [5] and dynamic snake convolutions [16], [17] improve tubular continuity, morphological thinning remains susceptible to fragmentation ($\beta_0 > 1$) and loops ($\beta_1 > 0$) under calcified plaques or low-contrast segments. Hybrid frameworks such as CorSegRec [7] reconnect broken skeletons via geodesic walks, whereas CNN orientation tracking [8], RefTr [9], and DeformCL [10] track or deform 3D centerline coordinates. However, local trackers can drift into adjacent veins, and direct 3D offset deformation without normal-plane projection or territory decoupling remains vulnerable to vertex bunching and cross-territory hijacking.

2.2 Sub-Voxel Distance Regression and Physiological Priors

Regressing continuous displacement vectors toward anatomical centerlines overcomes voxel discretization in curvilinear structure detection [8]. In parallel, physiological vascular scaling laws—most notably Murray's Law ($r^3_{\text{parent}} = \sum_k r^3_{\text{child},k}$) [18] and Huo–Kassab scaling [19], [20]—provide structural priors for distinguishing true bifurcations from noise. Our work synthesizes 3D sub-voxel displacement regression with dual-channel LCA/RCA decoupling and Murray-law geodesic pruning.

3 Methodology

As illustrated in Fig. 1, our 3D bilateral coronary reconstruction pipeline maps an input 128^3 CCTA volume $\mathbf{V}_{128} \in \mathbb{R}^{1\times128\times128\times128}$ with physical scale $\mathbf{s}_{\text{mm}} = (s_z, s_y, s_x) \in \mathbb{R}^3$ to a pair of topologically connected, acyclic 3D vascular trees $\mathcal{T}_{\text{LCA}} = (\mathcal{V}_{\text{LCA}}, \mathcal{E}_{\text{LCA}})$ and $\mathcal{T}_{\text{RCA}} = (\mathcal{V}_{\text{RCA}}, \mathcal{E}_{\text{RCA}})$ via four coupled stages ($M_1 \to M_4$).

3.1 Stage M_1: Multi-Scale 3D Pyramid Encoder and Tri-Directional Tubular Field Network

Given $\mathbf{V}_{128}$, the multi-scale 3D pyramid encoder extracts hierarchical features $\mathbf{F}_{64} \in \mathbb{R}^{16\times64^3}$, $\mathbf{F}_{32} \in \mathbb{R}^{32\times32^3}$, $\mathbf{F}_{16} \in \mathbb{R}^{64\times16^3}$, and global context $\mathbf{g}_{\text{ctx}} \in \mathbb{R}^{64}$ via the global context projection layer. In the 3D tubular decoder ($D_{\text{hid}} = 32$, $D_{\text{mid}} = \max(8, D_{\text{hid}}/2) = 16$), $\mathbf{F}_{32}$ is upsampled by the $32^3 \to 64^3$ transposed-convolution block (ConvTranspose3d($32 \to 32, k = 2, s = 2$) $\to$ GroupNorm$(4, 32)$ $\to$ GELU, $8,288$ parameters) to $\mathbf{U}_{32}$, concatenated with $\mathbf{F}_{64}$ as $\mathbf{C}_{64} = [\mathbf{U}_{32}, \mathbf{F}_{64}] \in \mathbb{R}^{48\times64^3}$, and decoded by the 64^3 fusion cascade (Conv3d($48 \to 32, k = 3, p = 1$) $\to$ GroupNorm$(4, 32)$ $\to$ GELU $\to$ Conv3d($32 \to 16, k = 3, p = 1$) $\to$ GroupNorm$(4, 16)$ $\to$ GELU $\to$ Conv3d($16 \to 1, k = 1$), $55,457$ parameters; $63,745$ base parameters) into base logits $\mathbf{L}_{\text{lumen}}$ and $\mathbf{P}_{\text{lumen}}(\mathbf{x}) = \sigma(\mathbf{L}_{\text{lumen}}(\mathbf{x}))$.

To overcome 64^3 discretization and LCA/RCA ambiguity while isolating 128^3 residual updates from destabilizing the $64^3/32^3$ backbone via explicit stop-gradient detachment ($\text{sg}(\cdot)$), we introduce four architectural branches:

1) **High-Resolution $128^3 \to 64^3$ Boundary Skip and Native 128^3 Residual Branch**: A stride-2 boundary block (Conv3d($1 \to 8, k = 3, s = 2, p = 1$) $\to$ GroupNorm$(2, 8)$ $\to$ GELU, 240 parameters) extracts high-resolution boundary cues $\mathbf{H}_{128} \in \mathbb{R}^{8\times64^3}$ from $\mathbf{V}_{128}$ to form $\mathbf{M}_{64} = [\mathbf{C}_{64}, \mathbf{H}_{128}] \in \mathbb{R}^{56\times64^3}$. In parallel, a native 128^3 convolutional stem (Conv3d($1 \to 8, k = 3, s = 1, p = 1$) $\to$ GroupNorm$(2, 8)$ $\to$ GELU, 240 parameters) fused with transposed-convolutional upsampled detached 64^3 features (ConvTranspose3d($56 \to 8, k = 2, s = 2$) $\to$ GroupNorm$(2, 8)$ $\to$ GELU applied to $\text{sg}(\mathbf{M}_{64})$, $3,608$ parameters) feeds the 128^3 residual tubular decoder (Conv3d($16 \to 8, k = 3, p = 1$) $\to$ GroupNorm$(2, 8)$ $\to$ GELU $\to$ Conv3d($8 \to 1, k = 1$), $3,489$ parameters; $7,337$ total 128^3 parameters) to predict $\Delta\mathbf{L}_{128} = 1.5\tanh(g_{128}([\mathbf{U}_{128}, \mathbf{S}_{128}]))$, $\mathbf{L}_{\text{lumen},128} = \text{Upsample}_{128}(\text{sg}(\mathbf{L}_{\text{lumen}})) + \Delta\mathbf{L}_{128}$, and $\mathbf{P}_{\text{lumen},128}(\mathbf{x}) = \sigma(\mathbf{L}_{\text{lumen},128}(\mathbf{x}))$.
2) **Continuous 3D Sub-Voxel Displacement Field**: A two-layer 3D regression head ($56 \to 16 \to 3$, $D_{\text{mid}} = 16$, $24,291$ parameters) maps $\mathbf{M}_{64}$ to a

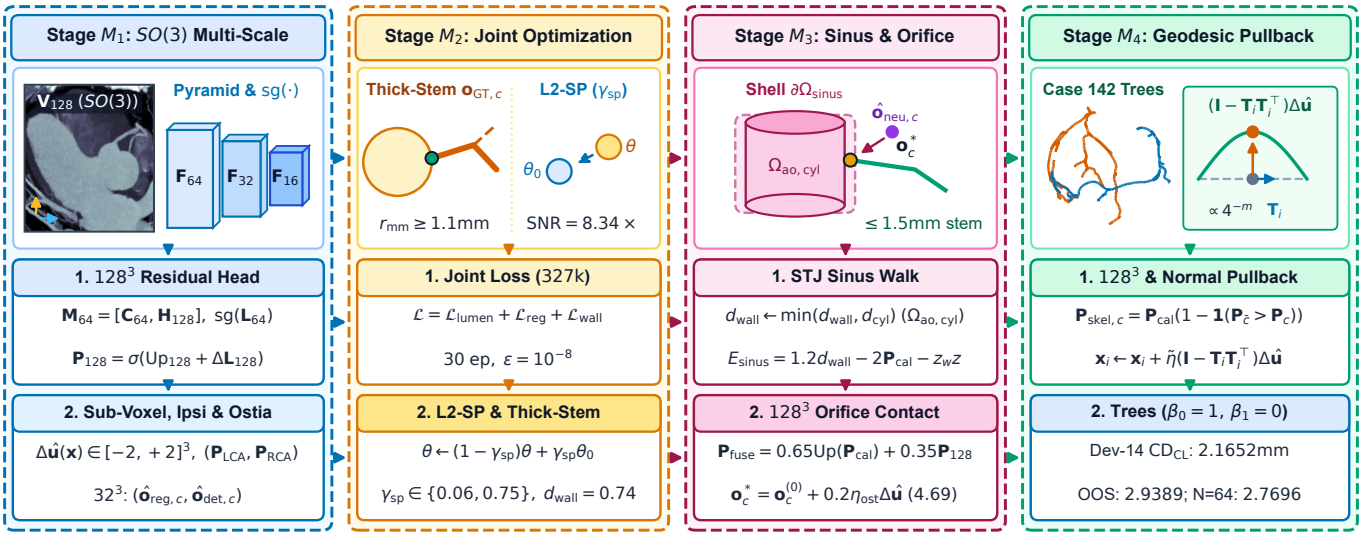

Fig. 1. Architectural overview of the proposed canonical $SO(3)$ $(Z_{\mathrm{IS}}, Y_{\mathrm{PA}}, X_{\mathrm{LR}})$ 3D bilateral coronary artery tree reconstruction pipeline across Stages $M_1 \rightarrow M_4$: (Stage M_1) multi-scale 3D pyramid encoder, $128^3 \rightarrow 64^3$ boundary skip, native 128^3 residual tubular branch ($\mathbf{P}_{\mathrm{lumen},128}$) with stop-gradient detachment sg(·), continuous sub-voxel displacement head ($\Delta\hat{\mathbf{u}}(\mathbf{x}) \in [-2,+2]^3$ mm), dual-channel ipsilateral head ($\mathbf{P}_{\mathrm{LCA}}, \mathbf{P}_{\mathrm{RCA}}$), and coarse 32^3 dual-sinus 3D ostium landmark detector ($\hat{\mathbf{o}}_{\mathrm{reg},c}, \hat{\mathbf{o}}_{\mathrm{det},c}$); (Stage M_2) single-loop 30-epoch multi-task optimization ($327,385$ active parameters) with decoupled L2-SP anchoring and connected thick-stem aortic-wall ostium supervision; (Stage M_3) coordinate-free cylindrical Valsalva-STJ wall calibration, conservative sinus-wall rooting, native-128^3 Valsalva-orifice contact expectation, and monotonic ostium pullback; and (Stage M_4) 128^3-coupled Riemannian minimal arborescence, pure contralateral inhibition, centripetal survival pruning, and 4-stage curvature-adaptive normal-plane pullback.

bounded 3D vector field ($\delta_{\max} = 2.0$ mm, zero-initialized final 1^3 layer):

$$\Delta\hat{\mathbf{u}}(\mathbf{x}) = \delta_{\max} \tanh\big(g_{\mathrm{disp}}(\mathbf{M}_{64})(\mathbf{x})\big) \in [-\delta_{\max}, +\delta_{\max}]^3. \quad (1)$$

3) **Dual-Channel Ipsilateral Decoupling**: Concatenating $\mathbf{M}_{64}$ with normalized coordinates $\mathbf{G}_{64}(\mathbf{x}) = (z, y, x) \in [0,1]^3$ (59 channels), a 3D decoupling head ($59 \rightarrow 16 \rightarrow 2$, zero-initialized final 1^3 layer, $25,570$ parameters) predicts residual logits $\Delta\mathbf{L}_{\mathrm{ipsi}}(\mathbf{x}) = (\Delta L_{\mathrm{LCA}}(\mathbf{x}), \Delta L_{\mathrm{RCA}}(\mathbf{x}))$:

$$\mathbf{P}_c(\mathbf{x}) = \sigma(\mathbf{L}_{\mathrm{lumen}}(\mathbf{x}) + \Delta L_c(\mathbf{x})), \quad c \in \{\mathrm{LCA}, \mathrm{RCA}\}. \quad (2)$$

4) **Coarse 32^3 Coordinate-Masked Dual-Sinus 3D Ostium Landmark Detector**: Operating on the downsampled 32^3 vascular crop, a dedicated 3D ostium landmark detector branch ($125,194$ parameters) combines coordinate-masked 3D convolutional features, keypoint attention, and differentiable spatial-to-numerical transform (DSNT) expectation with global context $\mathbf{g}_{\mathrm{ctx}}$ to predict dual-sinus normalized ostium coordinates $(\hat{\mathbf{o}}_{\mathrm{reg},c}, \hat{\mathbf{o}}_{\mathrm{det},c}) \in [0,1]^3$ and initial takeoff priors for $c \in \{\mathrm{LCA}, \mathrm{RCA}\}$.

3.2 Stage M_2: Single-Loop Recall-Preserving Multi-Task Optimization and Transparent Parameter Accounting

On the $N_{\mathrm{train}} = 35$ training volumes, each full-topology ground-truth centerline tree is partitioned via connected-component territorial partitioning across the 49 development/training volumes and the 50 out-of-sample volumes into connected arterial subtrees ($\mathcal{G}_{\mathrm{GT,LCA}}, \mathcal{G}_{\mathrm{GT,RCA}}$) and connected thick-stem aortic-wall ostium landmarks. Specifically, we select proximal trunk nodes with radius $r_{\mathrm{mm}} \geq \max(1.10\ \mathrm{mm}, P_{75}(r_{\mathrm{mm}}))$ [$\min r_{\mathrm{mm}} = 1.000$ mm] within $d_{\mathrm{wall}}(\mathbf{x}) + 0.5\,\phi_{\mathrm{side}}(\mathbf{x}) \leq \min(d_{\mathrm{wall}} + 0.5\,\phi_{\mathrm{side}}) + \delta_w$ where $\delta_w = 3.5/3.0$ mm for LCA/RCA (median $d_{\mathrm{wall}} = 0.7443$ mm). From these partitions, we precompute 64^3 distance fields $d_{\mathrm{LCA}}(\mathbf{x}), d_{\mathrm{RCA}}(\mathbf{x})$, Gaussian targets $Y_c(\mathbf{x}) = \exp(-d_c(\mathbf{x})^2/(2\sigma_L^2))$ ($\sigma_L = 2.0$ mm), masks $m_{\mathrm{pos},c}(\mathbf{x}) = \mathbb{I}(d_c(\mathbf{x}) \leq 2.5\ \mathrm{mm})$, $m_{\mathrm{contra},c}(\mathbf{x}) = \mathbb{I}(d_{\bar{c}}(\mathbf{x}) \leq 3.5\ \mathrm{mm} \wedge d_c(\mathbf{x}) > 4.5\ \mathrm{mm})$, $m_{\mathrm{bg}}(\mathbf{x}) = \mathbb{I}(d_{\mathrm{bi}}(\mathbf{x}) > 4.5\ \mathrm{mm})$, displacement targets $\Delta\mathbf{u}^*(\mathbf{x}) = \mathrm{clip}(\mathbf{p}_{\mathrm{GT}}(\mathbf{x}) - \mathbf{x}, -2.0, +2.0)$, cylindrical aortic-wall distance $\phi_{\mathrm{ao}}(\mathbf{x}) = d_{\mathrm{mm}}(\mathbf{x}, \partial\Omega_{\mathrm{cyl}})$, and 128^3 targets $Y_{128}(\mathbf{x}) = \exp(-d_{\mathrm{bi},128}(\mathbf{x})^2/(2\sigma_{128}^2))\mathbb{I}(d_{\mathrm{bi},128}(\mathbf{x}) \leq 2.5\ \mathrm{mm})$ ($\sigma_{128} = 1.65$ mm).

All $327,385$ active parameters are trained in a single 30-epoch cosine-annealed loop ($\mathcal{L}_{\mathrm{total}} = \mathcal{L}_{\mathrm{lumen}} + \mathcal{L}_{\mathrm{reg\text{-}gt}} + \mathcal{L}_{\mathrm{takeoff}}$) under AdamW ($\epsilon = 10^{-8}$ across all 7 parameter groups). To prevent representation drift, we apply decoupled L2-SP regularization ($40.0 \sum \|\theta - \theta_0\|_2^2$ on base encoder/lumen and 64^3 multi-task layers, $0.5 \sum \|\theta_{\mathrm{f6}} - \theta_{\mathrm{f6},0}\|_2^2$ on the final 1^3 lumen layer, $0.015 \sum \|\theta_{\mathrm{glob}} - \theta_{\mathrm{glob},0}\|_2^2$ on the global context projection layer, and $2.5 \sum \|\theta_{\mathrm{ost}} - \theta_{\mathrm{ost},0}\|_2^2$ on the 3D ostium detector). This is coupled with per-step EMA anchoring $\theta \leftarrow (1-\gamma_{\mathrm{sp}})\theta + \gamma_{\mathrm{sp}}\theta_0$ using $\gamma_{\mathrm{sp}} = 0.06$ on the final 1^3 lumen layer [lr $= 8.0\times10^{-4} \rightarrow 6.0\times10^{-4}$] and $\gamma_{\mathrm{sp}} = 0.75$ on remaining base encoder/lumen and 64^3 multi-task layers, while the global context projection, 128^3 residual layers, and ostium detector [lr $= 4.0 \times 10^{-5} \rightarrow 1.0 \times 10^{-5}$] adapt

without interpolation anchoring:

$$\begin{aligned}\mathcal{L}_{\text{lumen}} &= 0.25\,\mathcal{L}_{\text{BCE-vol}}(\mathbf{P}_{\text{lumen}}, \tilde{Y}_{\text{bi}}) + 1.00\,\mathcal{L}_{\text{pos-recall}} \\ &\quad + 85.0\,\mathcal{L}_{\text{far-focal}} + 0.15\,\mathcal{L}_{\text{Tversky}}^{(0.45,0.55)} + \mathcal{L}_{\text{L2-SP}} \\ &\quad + \mathcal{L}_{\text{disp}} + \mathcal{L}_{\text{ipsi}} + \mathcal{L}_{\text{lumen-128}}, \end{aligned} \tag{3}$$

$$\mathcal{L}_{\text{disp}} = 0.15\,\frac{\sum_{\mathbf{x},k} m_{\text{tube}}(\mathbf{x})\,\text{Smooth}L_1(\Delta\hat{u}_k - \Delta u_k^*;\beta_d)}{3\sum_{\mathbf{x}} m_{\text{tube}}(\mathbf{x})}, \tag{4}$$

$$\begin{aligned}\mathcal{L}_{\text{ipsi}} &= 0.16\left(\sum_{c,\mathbf{x}} w_{\text{ipsi},c}(\mathbf{x})\,\text{BCE}\big(\mathbf{P}_c(\mathbf{x}), Y_c(\mathbf{x})m_{\text{pos},c}(\mathbf{x})\big)\right. \\ &\quad + 1.8\,\frac{\sum_{c,\mathbf{x}} m_{\text{contra},c}(\mathbf{x})\,\text{ReLU}(\mathbf{P}_c(\mathbf{x}) - 0.08)^2}{\sum_{c,\mathbf{x}} m_{\text{contra},c}(\mathbf{x})} \\ &\quad \left. + 0.4\,\frac{\sum_{c,\mathbf{x}} m_{\text{bg}}(\mathbf{x})\,\text{ReLU}(\mathbf{P}_c(\mathbf{x}) - 0.12)^2}{2\sum_{\mathbf{x}} m_{\text{bg}}(\mathbf{x})}\right). \end{aligned} \tag{5}$$

Here $\mathcal{L}_{\text{BCE-vol}}$ uses $w_{\text{vox}}(\mathbf{x}) = 0.300\,w_{\text{pos}} + 0.100\,w_{\text{shell}} + 0.600\,w_{\text{far}}$ with $\tilde{Y}_{\text{bi}} = \min(1, 1.15\,Y_{\text{bi}})\mathbb{I}(d_{\text{bi}} \le 2.5\text{ mm})$ and a $1.40\times$ boost on $r \le 1.20$ mm inside w_{pos}. Vessel contrast is sharpened via $\mathcal{L}_{\text{pos-recall}} = \mathbb{E}_{Y_{\text{bi}}\ge 0.85}[\text{ReLU}(0.95 - \mathbf{P}_{\text{lumen}})^2]$, $\mathcal{L}_{\text{far-focal}} = \mathbb{E}_{d_{\text{bi}}>6.0\text{ mm}}[\text{ReLU}(\mathbf{P}_{\text{lumen}} - 0.035)^2]$ (Dev-14 median centerline probability 0.5810, far-field P_{95} 0.0696, SNR $= 8.34\times$), and $\mathcal{L}_{\text{Tversky}}^{(0.45,0.55)} = 1 - (2\text{TP}+1)/(2\text{TP}+0.45\text{FP}+0.55\text{FN}+1)$. High-resolution residual supervision uses $\mathcal{L}_{\text{lumen-128}} = 0.06\,(\mathcal{L}_{\text{BCE-128}} + 2.0\,\mathbb{E}_{d_{128}>6.0}[\text{ReLU}(\mathbf{P}_{\text{lumen},128} - 0.040)^2] + 0.02\,\mathbb{E}[\Delta\mathbf{L}_{128}^2])$ with $w_{128} \propto 0.35\,\mathbb{I}(d_{128} \le 2.5)(1 + 1.5\,\mathbb{I}(d_{128} \le 1.8 \wedge r_{128} \le 1.10\text{ mm})) + 0.45\,\mathbb{I}(3.0 < d_{128} \le 9.0 \wedge \mathbf{V}_{128} > 0.25) + 0.20\,\mathbb{I}(d_{128} > 6.0)$. Finally, $\mathcal{L}_{\text{reg-gt}} + \mathcal{L}_{\text{takeoff}}$ supervises ostium coordinates (0.50 global Smooth-L_1 [$\beta = 0.05$] + 0.12 millimeter Smooth-L_1 across $1.0\,\hat{\mathbf{o}}_{\text{reg},c} + 0.5\,\hat{\mathbf{o}}_{\text{key-cor},c} + 0.5\,\hat{\mathbf{o}}_{\text{key-base},c}$ [$\beta = 2.0$ mm]), wall consistency $\mathcal{L}_{\text{ost-wall}} = 0.05\sum_c(\text{Smooth}L_1(\text{ReLU}(|d_{\text{wall}}(\hat{\mathbf{o}}_{\text{reg},c}) - d_{\text{wall}}(\mathbf{o}_{\text{GT},c})| - 1.8\text{ mm}), 0; \beta = 1.0) + 0.5\,\text{Smooth}L_1(\text{ReLU}(|d_{\text{wall}}(\hat{\mathbf{o}}_{\text{key-cor},c}) - d_{\text{wall}}(\mathbf{o}_{\text{GT},c})| - 1.8\text{ mm}), 0; \beta = 1.0))$, and takeoff (0.08 weighted heatmap BCE + 0.15 cosine direction + 0.15 radius MSE), with $m_{\text{tube}}(\mathbf{x}) = \mathbb{I}(0.1 \le d_{\text{bi}}(\mathbf{x}) \le 4.0\text{ mm})$, $\beta_d = 0.5$ mm, and $w_{\text{ipsi},c} = 0.34\,\hat{m}_{\text{pos},c} + 0.44\,\hat{m}_{\text{contra},c} + 0.22\,\hat{m}_{\text{bg}}$.

Transparent Parameter Accounting: The bilateral arborescence network comprises $398,843$ total parameters ($71,458$ frozen step-flow parameters; $327,385$ active parameters trained with full end-to-end gradient flow in the joint lumen-ostium objective: $81,008$ in the 3D pyramid encoder, $121,183$ in the tubular decoder [$63,745$ base, $50,101$ 64^3 multi-task across the $128^3 \to 64^3$ boundary skip (240), sub-voxel displacement head ($24,291$), and dual-channel ipsilateral head ($25,570$), plus $7,337$ 128^3 residual across the 128^3 stem (240), $64^3 \to 128^3$ upsampler ($3,608$), and 128^3 residual head ($3,489$)], and $125,194$ in the 3D ostium landmark detector, with exact equality between active trainable parameters and the optimizer parameter set).

3.3 Stage M_3: Coordinate-Free Cylindrical Valsalva-STJ Wall Calibration, Conservative Sinus-Wall Rooting, Native-128^3 Orifice Contact Expectation, and Monotonic Ostium Pullback

For each artery $c \in \{\text{LCA}, \text{RCA}\}$, the 3D ostium landmark detector predicts $\hat{\mathbf{o}}_{\text{reg},c} = 0.45\,\hat{\mathbf{o}}_{\text{cor},c} + 0.52\,\hat{\mathbf{o}}_{\text{key-cor},c} + 0.03\,\sigma(\mathbf{g}_{\text{ctx},c}) \in [0,1]^3$ and $\hat{\mathbf{o}}_{\text{det},c} = 0.20\,\hat{\mathbf{o}}_{\text{dsnt},c} + 0.80\,\hat{\mathbf{o}}_{\text{reg},c} \in [0,1]^3$, passing $(\hat{\mathbf{o}}_{\text{reg},c}, \hat{\mathbf{o}}_{\text{det},c})$ to the solver with $\hat{\mathbf{o}}_{\text{neu},c} = 0.55\,\hat{\mathbf{o}}_{\text{reg},c} + 0.45\,\hat{\mathbf{o}}_{\text{det},c}$ along with aortic root center $\mathbf{c}_{\text{aorta}}$, 128^3 aortic-wall distance $d_{\text{wall}}(\mathbf{x})$, and sinotubular-extruded cylindrical wall distance $d_{\text{cyl}}(\mathbf{x}) = d_{\text{mm}}(\mathbf{x}, \partial\Omega_{\text{cyl}})$ (2D horizontal erosion above $z_{\text{cut}} = \lfloor 0.65 D_v \rfloor$ and downward STJ ring extrusion across $[\lfloor 0.45 D_v \rfloor, z_{\text{cut}})$). Across the physical Valsalva-STJ band $[z_{\text{cut}} - 16\text{ mm}, z_{\text{cut}} + 18\text{ mm}]$, we calibrate $d_{\text{wall}}(\mathbf{x}) \leftarrow \min(d_{\text{wall}}(\mathbf{x}), d_{\text{cyl}}(\mathbf{x}))$ and form $\Omega_{\text{ao, cyl}} = \Omega_{\text{ao, in}} \cup \{\mathbf{x} : z \in [\lfloor 0.45 D_v \rfloor, z_{\text{cut}}) \wedge (y,x) \in \mathcal{E}_2(\mathbf{M}_{\text{STJ}}) \wedge \mathbf{V}_{\text{sm}}(\mathbf{x}) > 0.42\}$ ($\mathcal{E}_2(\mathbf{M}_{\text{STJ}})$: 2-voxel eroded STJ slice). During bilateral sinus ostium localization, Stage-1 screening gates $\rho_{\text{ipsi},c}(\mathbf{x}) \ge \tau_\rho$ ($\tau_\rho = 0.45$, 0.25 fallback) and scores cranial components within cylindrical Valsalva bounds ($\Delta z_{\text{ao}} \in [-22, +24], \Delta y_{\text{ao}} \in [-24, +32], \Delta x_{\text{ao}} \in [-55, -3]$ mm for LCA; $\Delta z_{\text{ao}} \in [-40, +16], \Delta y_{\text{ao}} \in [+4, +58], \Delta x_{\text{ao}} \in [-8, +42]$ mm for RCA, with $w_{\text{wall}}(\mathbf{x}) = \exp(-\frac{1}{2}(\max(0, d_{\text{wall}}(\mathbf{x}) - 12.0)/10.0)^2)$ and $w_{\text{det},c}(\mathbf{x}) = 0.75 + 0.25\exp(-\frac{1}{2}(\max(0, d_{\text{neu},c}(\mathbf{x}) - 3.5)/15.0)^2)$ where $d_{\text{neu},c} = 0.55\,\|\mathbf{x} - \hat{\mathbf{o}}_{\text{reg},c}\|_{\text{mm}} + 0.45\,\|\mathbf{x} - \hat{\mathbf{o}}_{\text{det},c}\|_{\text{mm}}$). This is followed by the Stage-2 sinus-wall root walk:

$$\begin{aligned}E_{\text{sinus},c}(\mathbf{x}) &= 1.20\,d_{\text{wall}}(\mathbf{x}) - 2.00\,\mathbf{P}_{\text{cal}}(\mathbf{x}) - z_{w,c}\,z_{\text{mm}}(\mathbf{x}) \\ &\quad + 0.80\,\phi_{\text{sinus},c}(\mathbf{x} - \mathbf{c}_{\text{aorta}}) \\ &\quad + 0.06\,\max\big(0, \bar{d}_{\text{neu},c}(\mathbf{x}) - 6.0\big), \end{aligned} \tag{6}$$

where $\bar{d}_{\text{neu},c}(\mathbf{x}) = 0.50\,\|\mathbf{x} - \hat{\mathbf{o}}_{\text{reg},c}\|_{\text{mm}} + 0.50\,\|\mathbf{x} - \hat{\mathbf{o}}_{\text{det},c}\|_{\text{mm}}$, $(z_{w,0}, z_{w,1}) = (0.80, 0.55)$, and $\phi_{\text{sinus},c}$ penalizes displacement outside the sinus sector over trunk nodes within 28.0 mm satisfying $d_{\text{wall}} + 0.5\,\phi_{\text{sinus},c} \le \min(d_{\text{wall}} + 0.5\,\phi_{\text{sinus},c}) + \delta_{w,c}$ ($\delta_{w,0} = 2.5, \delta_{w,1} = 3.0$ mm). The walk retains $\mathbf{n}_{\text{init}}$ on caudal LCA walks ($\Delta z_{\text{walk}} < -2.0$ mm, $d_{\text{wall}}(\mathbf{n}_{\text{init}}) \le 4.0$ mm, $\|\mathbf{n}_{\text{init}} - \hat{\mathbf{o}}_{\text{neu},c}\|_{\text{mm}} \le 9.0$ mm, setting $d_{\text{cyl}}(\mathbf{x}_c^*) \leftarrow \min(d_{\text{cyl}}(\mathbf{x}_c^*), 2.0\text{ mm})$) or non-medial drift ($[d_{\text{wall}}(\mathbf{n}_{\text{init}}) \le 2.2\text{ mm} \vee (c = 0 \wedge d_{\text{wall}}(\mathbf{n}_{\text{init}}) \le 4.2\text{ mm} \wedge \|\mathbf{x}_c^* - \hat{\mathbf{o}}_{\text{neu},c}\|_{\text{mm}} > \|\mathbf{n}_{\text{init}} - \hat{\mathbf{o}}_{\text{neu},c}\|_{\text{mm}} + 6.0\text{ mm})]$, $\|\mathbf{n}_{\text{init}} - \hat{\mathbf{o}}_{\text{neu},c}\|_{\text{mm}} \le 8.5$ mm, $\Delta z_{\text{walk}} \le 4.0$ mm, and > 2.5 mm drift from $\hat{\mathbf{o}}_{\text{neu},c}$ without > 2.0 mm medial RCA convergence).

In Stage-3a conservative cylindrical sinus-wall rooting, after a 0.05 local wall nudge within 4.0 mm, detached roots ($d_{\text{cyl}}(\mathbf{x}_c^*) > 2.5$ mm or $c = 0 \wedge d_{\text{wall}}(\mathbf{x}_c^*) > 2.5$ mm) blend toward cylindrical-wall-regularized $\hat{\mathbf{o}}_{\text{wall},c} = 0.75\,\hat{\mathbf{o}}_{\text{neu},c} + 0.25\,\text{proj}_{\partial\Omega_{\text{cyl}}}(\hat{\mathbf{o}}_{\text{neu},c})$ ($2.2 < d_{\text{cyl}}(\hat{\mathbf{o}}_{\text{neu},c}) \le 6.5$ mm) with $w_{\text{fuse}} = (0.65 + 0.20\,g_{\text{gap}})$ if $\|\mathbf{x}_c^* - \hat{\mathbf{o}}_{\text{neu},c}\|_{\text{mm}} > 11.0$ mm else $(0.40 + 0.25\,g_{\text{gap}})$ where $g_{\text{gap}} = \text{clip}((\max(d_{\text{cyl}}(\mathbf{x}_c^*), d_{\text{wall}}(\mathbf{x}_c^*)) - 2.0)/3.0, 0, 1)$ when $\|\hat{\mathbf{o}}_{\text{reg},c} - \hat{\mathbf{o}}_{\text{det},c}\|_{\text{mm}} \le \tau_{\text{rd}}$ ($\tau_{\text{rd}} = 8.5$ mm, or 10.5 mm if $d_{\text{cyl}}(\mathbf{x}_c^*) > 6.0$ mm) and $d_{\text{cyl}}(\hat{\mathbf{o}}_{\text{neu},c}) \le 5.5$ mm (else cylindrical wall projection when $d_{\text{cyl}}(\mathbf{x}_c^*) > 3.5$ mm and projection distance ≤ 8.0 mm). Conversely, attached non-reverted roots ($d_{\text{cyl}}(\mathbf{x}_c^*) \le 2.5$ mm) remain untouched unless $\|\mathbf{x}_c^* - \hat{\mathbf{o}}_{\text{neu},c}\|_{\text{mm}} > 12.5$ mm, $\|\hat{\mathbf{o}}_{\text{reg},c} - \hat{\mathbf{o}}_{\text{det},c}\|_{\text{mm}} \le 5.5$ mm, and $d_{\text{cyl}}(\hat{\mathbf{o}}_{\text{neu},c}) \le 3.0$ mm ($w_{\text{fuse}} = 0.65$). In Stage-3b native-128^3 Valsalva-orifice contact expectation, on walks without caudal reversion when $\min(d_{\text{cyl}}(\mathbf{x}_c^*), d_{\text{wall}}(\mathbf{x}_c^*)) > 1.2$ mm, within a local 21^3-voxel window ($r_{\text{vox}} = 10$ at 128^3) we fuse $\mathbf{P}_{\text{fuse}} = 0.65\,\text{Upsample}_{128}(\mathbf{P}_{\text{cal}}) + 0.35\,\mathbf{P}_{\text{cal},128}$ on the 2-voxel Valsalva outer shell $\partial\Omega_{\text{sinus}} = \text{Dilate}_2(\Omega_{\text{ao, cyl}}) \setminus \Omega_{\text{ao, cyl}}$ ($d_{\text{cyl}} \le 2.2$ mm $\wedge\ \rho_{\text{ipsi},c} \ge 0.50 \wedge \|\mathbf{y} - \mathbf{x}_c^*\|_{\text{mm}} \le 6.5$ mm $\wedge\ \mathbf{P}_{\text{fuse}} \ge 0.34 \wedge \mathbf{V}_{128} \ge 0.38$), blending $\mathbf{o}_c^{(0)} \leftarrow 0.35\,\mathbf{x}_c^* + 0.65\,\hat{\mathbf{o}}_{\text{orif},c}$ over temperature-4.0 softmax scores $s_{\text{orif}}(\mathbf{y}) = 2.5\,\mathbf{P}_{\text{fuse}}(\mathbf{y}) + 0.8\,\mathbf{V}_{128}(\mathbf{y}) - 0.55\,d_{\text{cyl}}(\mathbf{y}) - 0.12\,\|\mathbf{y} - \mathbf{x}_c^*\|_{\text{mm}}$ when ≥ 3 contact voxels exist, followed by damped mono-

tonic sub-voxel projection ($\eta_{\text{ost}} = 0.65$):

$$\mathbf{o}_c^* = \mathbf{o}_c^{(0)} + 0.20\,\eta_{\text{ost}}\,\Delta\hat{\mathbf{u}}(\mathbf{o}_c^{(0)}), \tag{7}$$

accepted when $\mathbf{P}_{\text{lumen}}(\mathbf{o}_c^*) \geq \mathbf{P}_{\text{lumen}}(\mathbf{o}_c^{(0)})$ and $d_{\text{wall}}(\mathbf{o}_c^*) \leq d_{\text{wall}}(\mathbf{o}_c^{(0)}) + 0.5$ mm.

3.4 Stage M_4: Native-128^3 Residual Coupling, Pure Contralateral Inhibition, and Curvature-Adaptive Pullback

During Riemannian arborescence assembly, we suppress non-tubular high-intensity chambers via the cavity gate $\mathbf{G}_{\text{cav}}(\mathbf{x}) = \text{clip}((I_{\text{norm}}(\mathbf{x}) - 0.45)/0.35, 0, 1) \cdot \text{clip}((0.35 - \mathbf{V}(\mathbf{x}))/0.25, 0, 1) \cdot (1 - \mathbf{P}_{\text{cal}}(\mathbf{x}))^2$ and couple $\mathbf{P}_{128,\max}(\mathbf{x}) = \text{MaxPool}_{2\times2\times2}(\mathbf{P}_{\text{lumen},128})(\mathbf{x})$ via pre-skeletonization rescue ($\mathbf{P}_{\text{cal}}(\mathbf{x}) \leftarrow 0.85\,\mathbf{P}_{\text{cal}}(\mathbf{x}) + 0.15\,\mathbf{P}_{128,\max}(\mathbf{x})$ where $\rho_{\text{ipsi},c}(\mathbf{x}) \geq 0.82 \wedge \mathbf{P}_{\text{cal}}(\mathbf{x}) \geq 0.22 \wedge \mathbf{P}_{128,\max}(\mathbf{x}) \geq 0.40 \wedge \mathbf{P}_{128,\max}(\mathbf{x}) > \mathbf{P}_{\text{cal}}(\mathbf{x})$) and post-tree ridge pullback ($\mathbf{P}_{\text{smooth}}(\mathbf{x}) \leftarrow 0.88\,\mathbf{P}_{\text{smooth}}(\mathbf{x}) + 0.12\,\mathcal{G}_{0.35}(\mathbf{P}_{128,\max})(\mathbf{x})$). Prior to skeletonization ($\tau_{\text{snr}} = 0.25$), we apply binary contralateral exclusion and segment line-integral support gating:

$$\begin{aligned}\mathbf{P}_{\text{skel},c}(\mathbf{x}) = \mathbf{P}_{\text{cal}}(\mathbf{x}) \cdot \Big(1 - \mathbb{I}\big(\mathbf{P}_{\bar{c}} > \mathbf{P}_c \wedge \mathbf{P}_{\bar{c}} \geq 0.08 \\ \wedge\ \rho_{\text{ipsi},c} < 0.25\big)\Big),\end{aligned}$$

$$\begin{aligned}S_{\text{base}}(u,v) = 0.42\big(\mathbf{P}_{\text{cal}}(\mathbf{x}_u) + \mathbf{P}_{\text{cal}}(\mathbf{x}_v)\big) \\ + 0.10\,\text{mean}(\mathbf{P}_{\text{seg}}) + 0.06\,\min(\mathbf{P}_{\text{seg}}),\end{aligned} \tag{8}$$

scaling $S_{\text{base}}(u,v)$ by $0.85 + 0.15\,(\rho_{\text{seg},c}/0.18)$ only when $\rho_{\text{seg},c} < 0.18 \wedge \min(\mathbf{P}_{\text{seg}}) < 0.18$, and solving the Riemannian shortest-path tree rooted at $\mathbf{o}_c^*$ with resampled ≤ 1.5 mm geodesic inflow stems ($n_{\text{stem}} = \max(2, \lceil d_{\text{ost}}/1.5 \rceil)$) when $\|\mathbf{x}_1 - \mathbf{o}_c^*\|_2 > 3.5$ mm and Murray-law radius projection ($r^3_{\text{parent}} \approx \sum_k r^3_{\text{child},k}$). During inter-component bridging ($d > 12.0$ mm), contralateral components ($\rho_{\text{ipsi},c} < 0.35 \wedge \text{mean}(\mathbf{P}_{\bar{c}}) > 1.3\,\text{mean}(\mathbf{P}_c)$) are rejected, whereas right-coronary components ($x_{\text{mean}} \geq 0.55, \rho_{\text{ipsi,RCA}} \geq 0.75$) bridge calcified dropouts.

Curvature-Adaptive Normal-Plane Pullback and Multi-Stage Midpoint-Ridge Ascent: Candidate segments are evaluated at sub-voxel pullback points $\mathbf{q}_s = \mathbf{x}_i + s(\mathbf{x}_{i+1} - \mathbf{x}_i) + 0.5\,\eta_{\text{disp}}\,\Delta\hat{\mathbf{u}}(\mathbf{x}_i + s(\mathbf{x}_{i+1} - \mathbf{x}_i))$ ($s \in \{\frac{1}{4}, \frac{1}{2}, \frac{3}{4}\}$), blending support via $g_{\text{ip}}(s) = \text{clip}((\rho_{\text{ipsi},c}(\mathbf{q}_s) - 0.50)/0.35, 0, 1)$. Interior segments exceeding $\Delta s = 2.6$ mm (1.8 mm where $P_{\text{sub},c} \geq 0.55, \rho_{\text{ipsi},c} \geq 0.70$) are subdivided at their midpoint. For non-root nodes $\mathbf{x}_i$ ($i \geq 1$) with unit tangent $\mathbf{T}_i$, we iterate $K_{\text{disp}} = 3$ normal-plane steps coupled with $\mathbf{g}_{\perp,i} = (\mathbf{I} - \mathbf{T}_i\mathbf{T}_i^\top)\nabla((1 - w_{\text{ip, sub}})\mathbf{P}_{\text{smooth}}(\mathbf{x}_i) + w_{\text{ip, sub}}\mathbf{P}_{\text{ipsi, smooth},c}(\mathbf{x}_i))$ ($w_{\text{ip, sub}} = 0.20$), curvature gain $g_{\text{curv},s} = 1 + 0.20\,\kappa_{s,i}$, and chord damping $s_{\text{chord}} = \min(1.0, \Delta s/1.8)$ ($\tilde{\eta}_{\text{disp},i} = \eta_{\text{disp}}\,g_{\text{curv},s}\,s_{\text{chord}}$, $\tilde{\eta}_{g,i} = \eta_{g,\text{sub}}\,g_{\text{curv},s}\,s_{\text{chord}}$):

$$\begin{aligned}\mathbf{x}_i^{\text{cand}} = \mathbf{x}_i + \tilde{\eta}_{\text{disp},i}\left(\mathbf{I} - \mathbf{T}_i\mathbf{T}_i^\top\right)\Delta\hat{\mathbf{u}}(\mathbf{x}_i) \\ + \tilde{\eta}_{g,i}\tanh(2.5\,\|\mathbf{g}_{\perp,i}\|_2)\,\frac{\mathbf{g}_{\perp,i}}{\|\mathbf{g}_{\perp,i}\|_2 + 10^{-6}},\end{aligned} \tag{9}$$

where $\eta_{\text{disp}} = 0.65$ and $\eta_{g,\text{sub}} = 0.45\min(1, \eta_{\text{disp}}/0.65)$, accepting $\mathbf{x}_i^{\text{cand}}$ when $\mathbf{P}_{\text{smooth}}(\mathbf{x}_i^{\text{cand}}) \geq 0.85\,\mathbf{P}_{\text{smooth}}(\mathbf{x}_i)$, followed by normal-plane Laplacian smoothing ($w_{\text{smooth}} = 0.06$) and a four-stage midpoint subdivision and normal-plane ridge cascade ($m = 1, \ldots, 4$ down to $\Delta s \geq 1.06$ mm, $\alpha_{\text{curv},u} = 0.26$) with dual-point contralateral tip gating ($\rho_{\text{ipsi},c} \geq 0.75, P_{\text{sub},c} \geq 0.390$). Fixing $i = 0$ at $\mathbf{o}_c^*$ preserves 0.0000 mm root detachment and $\beta_0 = 1, \beta_1 = 0$.

Proposition 1 (Secant Sagitta Reduction under Multi-Stage Normal-Plane Subdivision): *For a regular vessel curve $\gamma : [0, \Delta s] \to \mathbb{R}^3$ with curvature $\kappa(s) \leq \kappa_{\max}$, an unsubdivided chord incurs midpoint sagitta error $e_{chord}(\Delta s) = \frac{1}{8}\kappa_{\max}(\Delta s)^2 + \mathcal{O}((\Delta s)^3)$. Recursively subdividing at the midpoint and projecting in $\mathbf{P}_\perp = \mathbf{I} - \mathbf{T}\mathbf{T}^\top$ across $m \geq 3$ stages reduces maximum residual sagitta by $4^m \geq 64$ to $e_{multi\text{-}stage}(\Delta s) \leq \frac{1}{8\cdot4^m}\kappa_{\max}(\Delta s)^2 + \varepsilon_\perp$.*

Unified Bottom-Up Centripetal Survival Functional: Terminal leaf trajectories t are pruned via a single-loop survival functional $\mathcal{S}_{\text{ipsi}}(t)$ coupling $\Delta\hat{\mathbf{u}}(\mathbf{x})$, $(\mathbf{P}_{\text{LCA}}, \mathbf{P}_{\text{RCA}})$, and $\mathbf{o}_c^*$:

$$\Delta P_{\text{disp}}(t) = \frac{1}{|t|}\sum_{\mathbf{x}\in t}\left(\mathbf{P}_{\text{smooth}}(\mathbf{x} + 0.5\,\Delta\hat{\mathbf{u}}(\mathbf{x})) - \mathbf{P}_{\text{smooth}}(\mathbf{x})\right), \tag{10}$$

$$\mathcal{S}_{\text{ipsi}}(t) = 1 - \left(\mathcal{H}_{\text{tort}}(t) + \mathcal{H}_{\text{terr}}(t) + \mathcal{H}_{\text{cent}}(t)\right), \tag{11}$$

where $\mathcal{H}_{\text{tort}}(t), \mathcal{H}_{\text{terr}}(t)$, and $\mathcal{H}_{\text{cent}}(t)$ penalize cross-territory, tortuous, and retrograde peri-ostial twigs without terminal coordinate boxes.

4 Experiments and Results

4.1 Dataset, Quarantine Firewall, and Evaluation Metrics

On the public 3D CCTA ImageCAS cohort [4], 35 volumes (< 129) form the training set, 14 unseen volumes (Cases 129–140, 142, 143; 28 trees) form the 5-fold cross-validation dev benchmark, 50 additional unseen volumes (Cases 251–300; 100 trees) form the zero-shot out-of-sample benchmark (pooled $N = 64$ unseen volumes / 128 trees), and Cases 201–250 remain strictly isolated in the locked confirmatory vault. We report bilateral and ipsilateral (LCA/RCA) CD_{CL}, uniform 1.0 mm arc-length $\text{CD}_{\text{CL}}^{\text{arc1mm}}$, P2G, G2P, HD_{95}, F1@1mm, F1@2mm, caliber-stratified Recall@2mm, Ostium Error, (β_0, β_1), and Root Detachment.

4.2 Quantitative Benchmark, Component Ablation, and Zero-Shot Generalization

Figure 2 and Tables 1–4 summarize the results:

1) **Comparison Against Classic and Modern Deep-Learning Baselines**: All five external baselines operate as controlled same-backbone implementations on the shared canonical $SO(3)$ 3D fields and full-topology ground-truth partitions (Table 1, Fig. 2b). 3D Seg+Thinning [5] yields 5.3926 ± 1.5744 mm CD_{CL} ($\text{CD}_{\text{CL}}^{\text{arc1mm}} = 5.0810$ mm, 8.02% F1@1mm). CorSegRec [7] (3.6919 ± 0.6773 mm, 11.92% F1@1mm), 1-Ch Minimal Path [8] (3.6159 ± 1.3352 mm, 12.36% F1@1mm), CNN-Tracker [8] (3.1151 ± 0.6172 mm, 21.49% F1@1mm), and DeformCL [10] (3.1663 ± 1.2977 mm, 34.96% F1@1mm) remain limited by 64^3 quantization and territory ambiguity. Our framework achieves 2.1652 ± 0.4686 mm bilateral CD_{CL} ($\text{CD}_{\text{CL}}^{\text{arc1mm}} = 2.2697 \pm 0.4863$ mm, 57.40% F1@1mm, 78.20% F1@2mm; proximal/intermediate/distal Rec@2mm = 83.40%/83.17%/68.07% vs. 35.69–72.43%/41.16–75.37%/33.96–59.32%), outperforming all five external baselines ($p \leq 0.00024$ on both CD_{CL} and $\text{CD}_{\text{CL}}^{\text{arc1mm}}$), including -1.0011 mm over DeformCL

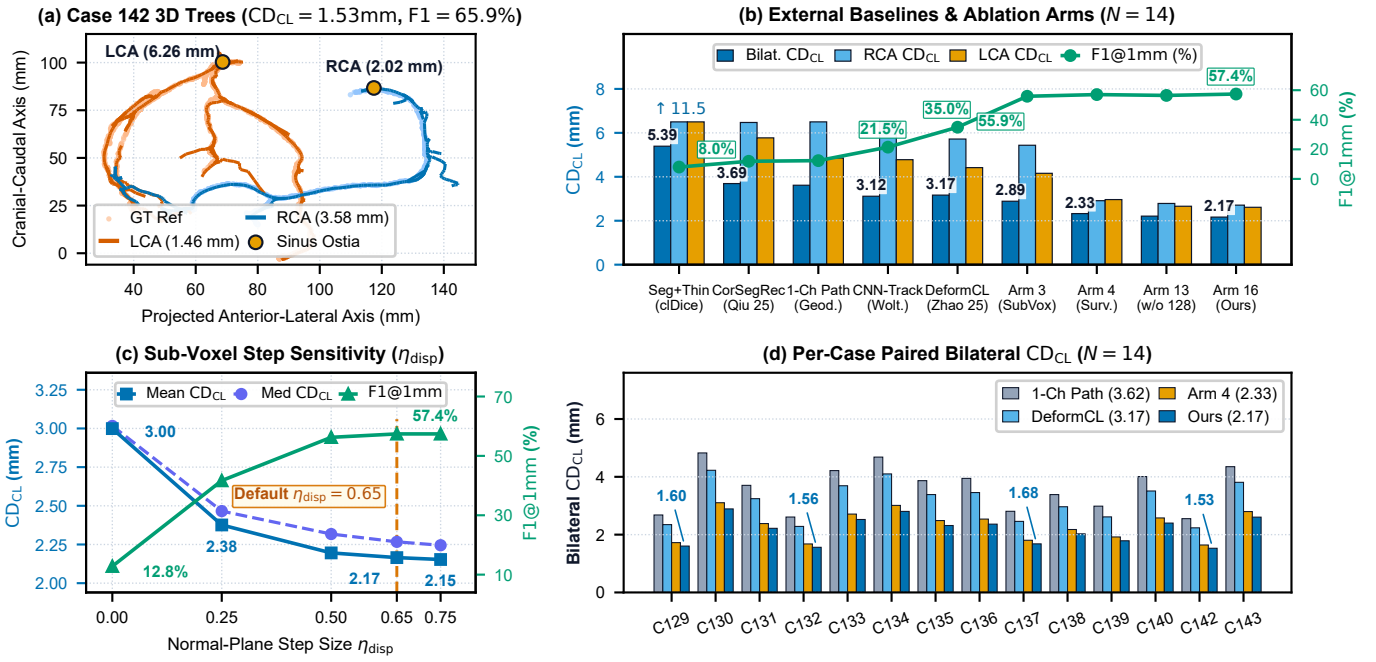

Fig. 2. Qualitative and quantitative evaluation of the proposed canonical $SO(3)$ $(Z_{\mathrm{IS}}, Y_{\mathrm{PA}}, X_{\mathrm{LR}})$ dual-channel ipsilateral, native 128^3 residual tubular decoder, conservative cylindrical sinus-wall and 128^3 Valsalva-orifice ostium rooting, and curvature-adaptive multi-stage coupled sub-voxel pullback arborescence framework across the $N = 14$ unseen ImageCAS development cases (28 coronary trees): (a) 3D bilateral coronary tree reconstruction on held-out Case 142 ($\mathrm{CD_{CL}} = 1.53$ mm, F1@1mm $= 65.9\%$, LCA/RCA $\mathrm{CD_{CL}} = 1.46/3.58$ mm, $\beta_0 = 1, \beta_1 = 0$ on both LCA and RCA trees); (b) comparison against five external classic and modern deep-learning baselines and orthogonal ablation progression across all 14 unseen volumes; (c) hyperparameter sensitivity analysis across normal-plane sub-voxel projection step size $\eta_{\mathrm{disp}} \in \{0.00, 0.25, 0.50, 0.65, 0.75\}$; and (d) per-case paired bilateral $\mathrm{CD_{CL}}$ comparison across all 14 unseen cases.

($p = 0.00024$ on Dev-14; $p = 1.62 \times 10^{-7}$ on OOS-50) and -0.9499 mm over CNN-Tracker ($p = 0.00024$).

2) **Single-Loop Training, 128^3 Residual Coupling, and Arc-Length De-Confounding**: Single-loop 30-epoch training improves displacement cosine similarity from 0.0000 to 0.7499, lowers near-vessel distance from 1.6796 mm to 1.0900 mm, raises ipsilateral/contralateral separation to 16.26×, and reaches Dev-14 median lumen probability 0.5810 with far-field $P_{95} = 0.0696$ (SNR $= 8.34\times$). In Table 2, Ipsilateral Decoupling Only (Arm 2) lowers $\mathrm{CD_{CL}}$ from 3.5955 mm to 3.0364 mm ($p = 0.00012$), while Sub-Voxel Pullback Only (Arm 3) raises F1@1mm to 55.89% (2.8876 mm $\mathrm{CD_{CL}}$). Combining contralateral inhibition and sub-voxel projection (Arm 4) yields 2.3255 mm, and the 2×2 Stage-$M_3 \times M_4$ 128^3 factorial ablation (Arms 13→16: 2.2090 → 2.1652 mm) confirms that Stage-M_3 128^3 orifice contact expectation reduces Dev-14 ostium error from 4.7929/5.2022 mm (Arms 13, 14) to 4.6880/4.9298 mm (Arms 15, 16) while Stage-M_4 128^3 coupling provides a statistically significant centerline gain (-0.0438 mm, $p = 0.02954$ vs. Arm 13; F1@1mm $+0.94\%$, $p = 0.00171$; $\mathrm{CD_{CL}^{arc1mm}}$ -0.0481 mm, $p = 0.04187$).

3) **Connected Thick-Stem Ostium Supervision and Conservative Sinus-Wall Rooting**: Coupling the coarse regression and DSNT ostium predictions ($\hat{\mathbf{o}}_{\mathrm{reg},c}, \hat{\mathbf{o}}_{\mathrm{det},c}$) with cylindrical Valsalva-STJ wall calibration, conservative cylindrical sinus-wall rooting, native-128^3 orifice contact expectation, geodesic inflow stems, and monotonic sub-voxel pullback reduces Dev-14 ostium mean error from 7.8880 mm (Arm 12, median 6.1787 mm) to 4.9298 mm (median 4.6880 mm, $16/28 \leq 5$ mm, $27/28 \leq 10$ mm, $p = 0.01328$) while significantly improving bilateral $\mathrm{CD_{CL}}$ (-0.0261 mm, $p = 0.02954$) and LCA/RCA $\mathrm{CD_{CL}}$ ($p = 0.01074/0.00403$) to 2.6118/2.7095 mm (median 2.2759/2.4685 mm).

4) **Zero-Shot Out-of-Sample Generalization ($N = 50$ OOS and Pooled $N = 64$ Unseen Volumes)**: Across Cases 251–300 (100 trees; Table 3, Part C), the frozen model achieves 2.9389 ± 1.2785 mm bilateral $\mathrm{CD_{CL}}$ (median 2.5642 mm, $\mathrm{CD_{CL}^{arc1mm}} = 3.1000 \pm 1.3381$ mm, F1@1/2mm $= 54.87\%/73.56\%$, LCA/RCA 3.6511 [3.2022] / 3.9831 [2.6776] mm, ostium median/mean 5.1815/7.5442 mm [$48/100 \leq 5$ mm, $78/100 \leq 10$ mm], runtime 207.4 s), significantly outperforming all five external baselines ($p = 5.33 \times 10^{-15}$ vs. Seg+Thinning, 6.54×10^{-10} vs. CorSegRec, 1.02×10^{-10} vs. 1-Ch Path, 7.24×10^{-7} vs. CNN-Tracker, and 1.62×10^{-7} vs. DeformCL). Across the pooled $N = 64$ unseen cohort (128 trees), it achieves 2.7696 ± 1.1919 mm $\mathrm{CD_{CL}}$ (median 2.4257 mm, $\mathrm{CD_{CL}^{arc1mm}} = 2.9184 \pm 1.2494$ mm, F1@1/2mm $= 55.42\%/74.58\%$, ostium median/mean 5.0017/6.9723 mm [$64/128 \leq 5$ mm, $105/128 \leq 10$ mm]) with 128/128 ($\beta_0 = 1$, $\beta_1 = 0$, 0.0000 mm detachment).

5 Discussion and Limitations

While our canonical $SO(3)$ framework substantially improves centerline precision and bilateral accuracy, several limitations bound our conclusions: (i) **Coarse 32^3 Ostium**

TABLE 1
14-Case 5-Fold Cross-Validation Bilateral and Ipsilateral Coronary CTA Reconstruction Benchmark ($N = 14$ Unseen Volumes, 28 Coronary Trees) in Canonical $SO(3)$ $(Z_{\mathsf{IS}}, Y_{\mathsf{PA}}, X_{\mathsf{LR}})$ Space. Compares Five External Classic and Modern Deep-Learning Baselines (evaluated as controlled same-backbone paradigm implementations on the shared 3D probability and displacement fields), Key Internal Evolution Stages, and Uniform 1.0 mm Arc-Length Resampled Chamfer Distance evaluated on identical full-topology physical millimeter coordinates.

Method / Paradigm	Mean CD_{CL} (mm)	Arc CD_{CL}^{arc1mm} (mm)	Med (mm)	P2G / G2P (mm)	HD_{95} (mm)	F1@1/2 (%)	LCA [Med] (mm)	RCA [Med] (mm)	Ost Med/Mean (mm)	Topo (β_0, β_1)
Hist. 1-Tree Baseline	16.18 ± 1.50	—	16.17	17.52/14.84	37.54	—	—	—	14.29/16.40	14/14
3D Seg + Skel. [5]	5.3926 ± 1.5744	5.0810 ± 1.5099	5.0088	7.32/3.47	25.65	8.02/34.64	7.62 [6.54]	11.47 [9.69]	6.22/7.91	28/28
CorSegRec Walk [7]	3.6919 ± 0.6773	3.7053 ± 0.6896	3.6937	3.93/3.45	16.97	11.92/44.20	5.77 [5.62]	6.47 [4.95]	**4.69**/**4.93**	28/28
1-Ch Minimal Path [8]	3.6159 ± 1.3352	3.6643 ± 1.3631	3.1586	3.33/3.90	19.32	12.36/51.87	4.86 [3.84]	6.50 [4.08]	6.22/7.91	28/28
Deep CNN Tracker [8]	3.1151 ± 0.6172	3.0422 ± 0.6160	3.0504	3.49/2.74	15.14	21.49/60.39	4.78 [3.26]	8.78 [8.01]	**4.69**/4.99	28/28
DeformCL Offset [10]	3.1663 ± 1.2977	3.2375 ± 1.3346	2.7666	2.84/3.49	19.37	34.96/68.16	4.42 [3.37]	5.72 [3.66]	**4.69**/**4.93**	28/28
1-Ch Geodesic Stage	3.5955 ± 1.2987	3.6439 ± 1.3269	3.1586	3.32/3.87	19.31	12.40/51.90	4.84 [3.83]	6.22 [4.06]	4.94/5.26	28/28
Dual-Ch Survival Stage	3.0364 ± 0.4247	3.0643 ± 0.4522	3.0843	3.31/2.76	12.99	12.66/52.96	3.62 [3.04]	3.69 [3.31]	4.94/5.26	28/28
Sinus-Centripetal Stage	2.3255 ± 0.4907	2.3792 ± 0.5054	2.3661	2.52/2.14	12.99	57.03/76.38	2.96 [2.37]	2.91 [2.55]	4.94/5.26	28/28
Sub-Voxel Ost+Bridge	2.2568 ± 0.4694	2.3316 ± 0.4892	2.3340	2.40/2.11	12.41	**58.38**/76.81	2.81 [2.30]	2.84 [2.62]	**4.69**/5.12	28/28
Two-Stage Midpoint	2.2398 ± 0.4563	2.3359 ± 0.4869	2.3384	2.36/2.12	12.20	56.99/77.22	2.74 [2.25]	2.84 [2.62]	**4.69**/5.12	28/28
Coherent Two-Stage	2.2334 ± 0.4517	2.3322 ± 0.4823	2.3353	2.34/2.12	12.10	56.62/77.36	2.72 [2.24]	2.82 [2.61]	4.79/5.20	28/28
Curvature 3-Stage	2.2177 ± 0.4427	2.3240 ± 0.4771	2.3212	2.31/2.13	11.94	56.46/77.55	2.68 [**2.21**]	2.80 [2.63]	4.79/5.20	28/28
Proposed Full	$\mathbf{2.1652 \pm 0.4686}$	$\mathbf{2.2697 \pm 0.4863}$	**2.2672**	**2.22**/**2.12**	**11.49**	57.40/**78.20**	**2.61** [2.28]	**2.71** [**2.47**]	**4.69**/**4.93**	**28/28**

TABLE 2
Orthogonal Component Ablation Study and Uniform 1.0 mm Arc-Length De-Confounding across the 14 Held-Out Development Cases (28 Coronary Trees) in Canonical $SO(3)$ $(Z_{\mathsf{IS}}, Y_{\mathsf{PA}}, X_{\mathsf{LR}})$ Coordinates. Every Ablation Arm Executes Live on the Canonical Checkpoint and Full-Topology Ground-Truth Partition.

Ablation Arm	Skip $+\Delta\hat{\mathbf{u}}$	Dual Ipsi	Cent. Surv.	Ost+ Brg	Pull./ 128^3	Bilat. Mean CD_{CL} (mm)	1mm Arc CD_{CL}^{arc1mm} (mm)	Med (mm)	P2G/G2P (mm)	HD_{95} (mm)	F1@1/2mm (%) [LCA/RCA/Ost]
1. Recombined 1-Ch Baseline	—	—	—	—	—	3.5955 ± 1.2987	3.6439 ± 1.3269	3.1586	3.32/3.87	19.31	12.4/51.9 [4.84/6.22/4.94]
2. Ipsilateral Decoupling Only	—	✓	✓	—	—	3.0364 ± 0.4247	3.0643 ± 0.4522	3.0843	3.31/2.76	12.99	12.7/53.0 [3.62/3.69/4.94]
3. Sub-Voxel Pullback Only	✓	—	—	—	—	2.8876 ± 1.3215	2.9584 ± 1.3527	2.5882	2.55/3.23	19.35	55.9/74.1 [4.16/5.44/4.94]
4. Centripetal Survival Pruning	✓	✓	✓	—	—	2.3255 ± 0.4907	2.3792 ± 0.5054	2.3661	2.52/2.14	12.99	57.0/76.4 [2.96/2.91/4.94]
5. Sub-Voxel Ostium Only	✓	✓	✓	Ost	—	2.3250 ± 0.4903	2.3792 ± 0.5056	2.3661	2.51/2.14	12.99	57.1/76.4 [2.96/2.91/**4.69**]
6. Pullback Bridge Only	✓	✓	✓	Brg	—	2.2571 ± 0.4696	2.3316 ± 0.4889	2.3340	2.40/2.11	12.41	**58.4**/76.8 [2.81/2.84/4.94]
7. Joint Ostium + Bridge	✓	✓	✓	✓	—	2.2568 ± 0.4694	2.3316 ± 0.4892	2.3340	2.40/2.11	12.41	**58.4**/76.8 [2.81/2.84/**4.69**]
8. Single-Stage Ridge Pullback	✓	✓	✓	✓	1-Stg	2.2691 ± 0.4633	2.3429 ± 0.4841	2.3484	2.42/2.12	12.40	57.1/77.0 [2.81/2.87/**4.69**]
9. Two-Stage Coupled Pullback	✓	✓	✓	✓	2-Stg	2.2398 ± 0.4563	2.3359 ± 0.4869	2.3384	2.36/2.12	12.20	57.0/77.2 [2.74/2.84/**4.69**]
10. Coherent Two-Stage Pullback	✓	✓	✓	✓	Coh-2	2.2334 ± 0.4517	2.3322 ± 0.4823	2.3353	2.34/2.12	12.10	56.6/77.4 [2.72/2.82/4.79]
11. Curvature 3-Stage Pullback	✓	✓	✓	✓	Crv-3	2.2177 ± 0.4427	2.3240 ± 0.4771	2.3212	2.31/2.13	11.94	56.5/77.6 [2.68/2.80/4.79]
12. w/o Cylindrical Sinus Rooting	✓	✓	✓	Raw	Full-4	2.1913 ± 0.4953	2.2963 ± 0.5093	2.2687	2.23/2.16	11.69	57.2/78.0 [2.64/2.77/6.18]
13. w/o Stage-M_3 & M_4 128^3	✓	✓	✓	✓	No-128^3	2.2090 ± 0.4402	2.3178 ± 0.4727	2.3188	2.29/2.13	11.86	56.5/77.6 [2.66/2.79/4.79]
14. w/o Stage-M_3 128^3 Orifice	✓	✓	✓	✓	$+M_4$	$\mathbf{2.1650 \pm 0.4687}$	$\mathbf{2.2694 \pm 0.4861}$	**2.2672**	**2.22**/**2.11**	**11.49**	57.4/**78.2** [**2.61**/**2.71**/4.79]
15. w/o Stage-M_4 128^3 Coupling	✓	✓	✓	✓	$+M_3$	2.2092 ± 0.4405	2.3181 ± 0.4736	2.3188	2.29/2.13	11.86	56.5/77.7 [2.66/2.79/**4.69**]
16. **Proposed Full Framework**	✓	✓	✓	✓	**Full-4**	2.1652 ± 0.4686	2.2697 ± 0.4863	**2.2672**	**2.22**/**2.12**	**11.49**	57.4/**78.2** [**2.61**/**2.71**/**4.69**]

Landmark Detector Generalization Gap and Zero-Shot Ostium Tail: While zero-shot transfer to Cases 251–300 confirms generalization without retuning ($p \leq 7.24 \times 10^{-7}$ vs. external baselines, 5.1815 mm median ostium error, 78/100 ostia ≤ 10 mm), the 22/100 tail > 10 mm and RCA mean-to-median skew (3.9831 vs. 2.6776 mm) reflect both severe motion/calcification and the upstream generalization gap of the coarse 32^3 coordinate-masked 3D ostium landmark detector (5.15 mm median error on $N_{\text{train}} = 35$ vs. 6.80 mm on Dev-14 and 7.81 mm on OOS-50 under the 35-volume/70-ostium regime); (ii) **Distal Apical Completeness**: Distal recall (Distal Rec@2mm $= 68.07\%$ on Dev-14; 62.89% on OOS-50) remains bounded by partial-volume attenuation in sub-millimeter twigs ($r < 0.75$ mm); and (iii) **Decoupled Graph Assembly**: The 3D pyramid encoder, tubular segmentation decoder, and 3D ostium landmark detector are trained via multi-task volumetric and centerline losses, whereas Riemannian shortest-path assembly operates at inference without discrete graph backpropagation.

6 Conclusion

We presented a 3D bilateral coronary tree reconstruction framework in canonical $SO(3)$ $(Z_{\mathsf{IS}}, Y_{\mathsf{PA}}, X_{\mathsf{LR}})$ space combining a $128^3 \rightarrow 64^3$ boundary skip, a native 128^3 residual tubular decoder, a continuous 3D sub-voxel displacement field $\Delta\hat{\mathbf{u}}(\mathbf{x})$, and dual-channel ipsilateral LCA/RCA decoupling trained in a single 30-epoch loop ($327,385$ active parameters, $\epsilon = 10^{-8}$). Coupled with cylindrical Valsalva-STJ wall calibration, conservative cylindrical sinus-wall rooting, native-128^3 orifice contact expectation, geodesic inflow stems, 128^3 residual coupling, pure contralateral inhibition, and curvature-adaptive normal-plane pullback, the framework achieves 2.1652 ± 0.4686 mm bilateral CD_{CL} (4.6880/4.9298 mm median/mean ostium error, $27/28 \leq 10$ mm) across 14 unseen dev volumes and 2.9389 ± 1.2785 mm across 50 zero-shot OOS volumes (pooled $N = 64$ mean 2.7696 ± 1.1919 mm, median 2.4257 mm, ostium median/mean 5.0017/6.9723 mm, $128/128$ $\beta_0 = 1, \beta_1 = 0$).

References

[1] C. A. Taylor, T. A. Fonte, and J. K. Min, "Computational fluid dynamics applied to cardiac computed tomography for noninvasive quantification of fractional flow reserve: scientific basis," *Journal of the American College of Cardiology*, vol. 61, no. 22, pp. 2233–2241, 2013.

[2] J. K. Min, J. Leipsic, M. J. Pencina, D. S. Berman, B.-K. Koo, C. van Mieghem, A. Erglis, F. Y. Lin, A. M. Dunning, P. Apruzzese *et al.*, "Diagnostic accuracy of fractional flow reserve from anatomic ct angiography: Defacto study," *JAMA*, vol. 308, no. 12, pp. 1237–1245, 2012.

[3] B. L. Nørgaard, J. Leipsic, S. Gaur, S. Seneviratne, B. S. Ko, H. Ito, J. M. Jensen, L. Mauri, B. De Bruyne, M. Bergmann *et al.*, "Diagnostic performance of noninvasive fractional flow reserve derived from coronary computed tomography angiography in suspected coronary artery disease: the nxt trial," *Journal of the American College of Cardiology*, vol. 63, no. 12, pp. 1145–1155, 2014.

[4] A. Zeng, C. Wu, G. Lin, W. Xie, J. Hong, M. Huang, J. Zhuang, S. Bi, D. Pan, N. Ullah, K. N. Khan, T. Wang, Y. Shi, X. Li, and X. Xu, "Imagecas: A large-scale dataset and benchmark for coronary artery segmentation based on computed tomography angiography images," *Computerized Medical Imaging and Graphics*, vol. 109, p. 102287, 2023.

[5] S. Shit, J. C. Paetzold, A. Sekuboyina, I. Ezhov, A. Unger, A. Zhylka, J. P. Pluim, U. Bauer, and B. H. Menze, "cldice - a novel topology-preserving loss function for tubular structure segmentation," in *Proceedings of the IEEE/CVF Conference on Computer Vision and Pattern Recognition (CVPR)*, 2021, pp. 16 560–16 569.

TABLE 3
Paired Non-Parametric Statistical Significance ($N = 14$ Unseen Dev Cases), Sub-Voxel Step-Size (η_{disp}) Sensitivity Analysis, and Large-Cohort Zero-Shot Out-of-Sample Generalization Across $N = 50$ Unseen Volumes (Cases 251–300, 100 Coronary Trees) and Pooled $N = 64$ Unseen Cohort (128 Trees) in Canonical $SO(3)$ $(Z_{\text{IS}}, Y_{\text{PA}}, X_{\text{LR}})$ Space.

Part A: Paired Statistical Significance of Proposed Full Framework vs. External & Internal Baselines ($N = 14$ Dev Volumes)

Comparison Pair	$\Delta\text{CD}_{\text{CL}}$	95% CI	Wilc. p	ΔF1@1	95% CI	Wilc. p	$\Delta\text{L}/\Delta\text{R}$ ($p_{\text{L}}/p_{\text{R}}$)
vs. 3D Seg+Skel. [5]	-3.2274	$[-4.03, -2.50]$	**0.00012**	$+49.38$	$[+45.6, +52.9]$	**0.00012**	$-5.01/-8.76$ (1e-4)
vs. CorSegRec [7]	-1.5267	$[-1.81, -1.17]$	**0.00024**	$+45.48$	$[+41.0, +49.7]$	**0.00012**	$-3.16/-3.76$ (12/4e-4)
vs. 1-Ch Path [8]	-1.4507	$[-2.14, -0.91]$	**0.00012**	$+45.04$	$[+40.9, +49.1]$	**0.00012**	$-2.24/-3.79$ (1e-4)
vs. CNN Tracker [8]	-0.9499	$[-1.20, -0.69]$	**0.00024**	$+35.91$	$[+31.7, +40.0]$	**0.00012**	$-2.17/-6.07$ (9/4e-4)
vs. DeformCL [10]	-1.0011	$[-1.65, -0.48]$	**0.00024**	$+22.43$	$[+20.1, +24.9]$	**0.00012**	$-1.81/-3.01$ (2/1e-4)
vs. Recombined 1-Ch Base	-1.4303	$[-2.11, -0.90]$	**0.00012**	$+45.00$	$[+40.9, +49.1]$	**0.00012**	$-2.23/-3.51$ (1e-4)
vs. Ipsilateral Only	-0.8712	$[-0.97, -0.77]$	**0.00012**	$+44.74$	$[+40.6, +48.7]$	**0.00012**	$-1.01/-0.98$ (1e-4)
vs. Sub-Voxel Pullback Only	-0.7224	$[-1.40, -0.19]$	**0.01074**	$+1.51$	$[+0.07, +2.8]$	0.10400	$-1.55/-2.73$ (.013/.035)
vs. Centripetal Survival	-0.1603	$[-0.26, -0.08]$	**0.00232**	$+0.36$	$[-0.6, +1.2]$	0.24121	$-0.35/-0.20$ (2e-4/.091)
vs. Joint Ostium+Bridge	-0.0916	$[-0.16, -0.03]$	**0.01343**	-0.99	$[-2.0, -0.1]$	**0.04187**	$-0.19/-0.13$ (.001/.068)
vs. Single-Stage Ridge	-0.1039	$[-0.17, -0.04]$	**0.00525**	$+0.31$	$[-0.2, +0.7]$	0.10400	$-0.19/-0.16$ (.002/.042)
vs. w/o Cyl. Sinus Rooting	-0.0261	$[-0.07, -0.0005]$	**0.02954**	$+0.17$	$[-0.02, +0.4]$	0.16715	$-0.03/-0.06$ (.011/.004)
vs. w/o M_3 & M_4 128^3	-0.0438	$[-0.09, +0.002]$	**0.02954**	$+0.94$	$[+0.5, +1.4]$	**0.00171**	$-0.05/-0.08$ (.194/.011)
vs. w/o M_4 128^3 Coupling	-0.0440	$[-0.09, +0.002]$	0.06763	$+0.90$	$[+0.5, +1.3]$	**0.00232**	$-0.05/-0.08$ (.194/.020)

Part B: Sensitivity Analysis Across Sub-Voxel Step Size $\eta_{\text{disp}} \in \{0.00, 0.25, 0.50, 0.65, 0.75\}$ ($N = 14$ Dev Volumes)

Step Size η_{disp}	Mean CD_{CL}	Arc $\text{CD}_{\text{CL}}^{\text{arc1mm}}$	P2G/G2P	HD_{95}	F1@1/2	LCA [Med]	RCA [Med]
$\eta_{\text{disp}} = 0.00$	2.9990 ± 0.4278	3.0261 ± 0.4501	3.25/2.75	12.36	12.81/53.72	3.58 [3.11]	3.62 [3.12]
$\eta_{\text{disp}} = 0.25$	2.3762 ± 0.4448	2.4758 ± 0.4632	2.49/2.27	11.55	41.67/74.94	2.78 [2.54]	2.96 [2.64]
$\eta_{\text{disp}} = 0.50$	2.1956 ± 0.4559	2.3044 ± 0.4765	2.26/2.13	11.49	56.25/77.78	2.65 [2.35]	2.73 [2.47]
$\eta_{\text{disp}} = \mathbf{0.65}$ **(Def.)**	2.1652 ± 0.4686	2.2697 ± 0.4863	2.22/2.12	11.49	**57.40/78.20**	2.61 [2.28]	**2.71 [2.47]**
$\eta_{\text{disp}} = 0.75$	$\mathbf{2.1529 \pm 0.4604}$	$\mathbf{2.2520 \pm 0.4680}$	**2.19/2.11**	**11.35**	**57.40**/78.06	**2.57 [2.25]**	2.72 [2.47]

Part C: Zero-Shot Out-of-Sample Generalization Across $N = 50$ Unseen Volumes (Cases 251–300) & Pooled $N = 64$ Cohort

OOS Paradigm	Mean CD_{CL}	Arc $\text{CD}_{\text{CL}}^{\text{arc1mm}}$	Med/P2G/G2P	HD_{95}	F1@1/2	LCA/RCA [Med]	Ost Med/Mean
3D Seg+Skel. [5]	6.1447 ± 1.4060	5.8079 ± 1.4094	6.15/8.95/3.34	30.17	8.16/34.34	9.3/10.8 [8.7/9.9]	7.49/9.23 (5e-15)
CorSegRec [7]	4.1358 ± 1.0191	4.1546 ± 1.0233	3.99/5.04/3.23	21.18	13.52/46.34	7.3/6.5 [6.0/5.9]	**5.18/7.54** (7e-10)
1-Ch Path [8]	3.9266 ± 1.4076	3.9666 ± 1.4013	3.69/4.36/3.49	19.87	14.50/53.21	6.5/6.6 [5.1/3.7]	7.49/9.23 (1e-10)
CNN Tracker [8]	3.9347 ± 1.0256	3.8488 ± 1.0154	3.79/4.65/3.22	21.45	21.93/57.34	5.2/7.6 [4.1/6.3]	5.30/7.59 (7e-07)
DeformCL [10]	3.5344 ± 1.4244	3.5975 ± 1.4191	3.27/3.96/3.11	19.81	35.61/65.63	6.1/5.9 [4.7/3.2]	**5.18/7.54** (2e-07)
Proposed ($N = 50$)	$\mathbf{2.9389 \pm 1.2785}$	$\mathbf{3.1000 \pm 1.3381}$	**2.56/3.12/2.76**	**16.89**	**54.87/73.56**	**3.7/4.0 [3.2/2.7]**	**5.18/7.54** ($78 \leq 10$)
Pooled ($N = 64$)	2.7696 ± 1.1919	2.9184 ± 1.2494	2.43/2.92/2.62	15.71	55.42/74.58	3.4/3.7 [2.7/2.6]	5.00/6.97 ($64 \leq 5$)

TABLE 4
5-Fold Cross-Validation Summary and Per-Case Performance Breakdown on the 14 Held-Out ImageCAS Development Cases in Canonical $SO(3)$ $(Z_{\text{IS}}, Y_{\text{PA}}, X_{\text{LR}})$ Space.

Case ID (Fold)	Total Nodes	Bilat. CD_{CL} (mm)	P2G (mm)	G2P (mm)	HD_{95} (mm)	LCA CD_{CL} (mm)	RCA CD_{CL} (mm)	LCA Ost (mm)	RCA Ost (mm)	Prox Rec@2 (%)	Time (s)
Case 129 (Fold 0)	897	1.60	1.44	1.77	6.43	1.65	1.53	4.06	4.76	89.7	2.67
Case 133 (Fold 0)	697	2.52	2.06	2.99	12.27	6.53	4.25	3.76	2.89	69.3	2.43
Case 134 (Fold 0)	478	2.80	2.73	2.87	12.43	2.65	3.06	1.36	6.67	67.5	2.19
Case 130 (Fold 1)	1103	2.89	3.29	2.49	18.94	2.22	5.70	4.78	2.90	100.0	2.52
Case 131 (Fold 1)	1150	2.22	2.52	1.92	11.26	2.33	2.56	7.68	7.20	66.5	2.92
Case 135 (Fold 1)	1154	2.32	3.23	1.40	16.70	2.38	3.54	2.16	1.30	75.2	2.84
Case 132 (Fold 2)	807	1.56	1.53	1.59	6.00	1.59	1.69	8.95	2.32	97.8	2.33
Case 136 (Fold 2)	929	2.36	2.25	2.48	11.66	3.52	2.05	2.24	2.38	81.1	2.62
Case 138 (Fold 2)	815	2.03	2.09	1.96	11.13	1.73	2.38	8.42	5.87	85.6	2.28
Case 137 (Fold 3)	839	1.68	2.16	1.20	9.28	1.96	1.43	5.41	7.17	81.3	2.28
Case 139 (Fold 3)	976	1.79	1.76	1.81	8.67	1.85	2.65	4.62	6.18	100.0	2.77
Case 142 (Fold 3)	1010	1.53	1.90	1.16	10.20	1.46	3.58	6.26	2.02	98.9	2.41
Case 140 (Fold 4)	1032	2.40	1.74	3.06	13.89	4.02	1.35	9.98	3.49	94.2	2.52
Case 143 (Fold 4)	938	2.61	2.31	2.90	12.01	2.68	2.16	1.00	12.21	60.5	3.00
Cohort Mean $\pm$ SD	916 ± 182	$\mathbf{2.17 \pm 0.47}$	**2.22**	**2.12**	$\mathbf{11.49 \pm 3.52}$	$\mathbf{2.61 \pm 1.34}$	$\mathbf{2.71 \pm 1.23}$	Med **4.69** / Mean **4.93**		**83.4**	2.56

[6] M. Owusu-Ansah, K. Lee, V. Venugopal, M. Jawaid, W. Duan, and J. Brown, "Same branches, different trees: A bifurcation connectedness metric for coronary artery segmentation and ffr-ct decision agreement," *arXiv preprint arXiv:2607.28327*, 2026.

[7] Y. Qiu, D. Shan, Y. Wang, P. Dong, D. Wu, X. Yang, Q. Hong, and D. Shen, "A topology-preserving three-stage framework for fully-connected coronary artery extraction," *Medical Image Analysis*, vol. 103, p. 103578, 2025.

[8] J. M. Wolterink, R. W. van Hamersvelt, M. A. Viergever, T. Leiner, and I. Išgum, "Coronary artery centerline extraction in cardiac ct angiography using a cnn-based orientation classifier," *Medical Image Analysis*, vol. 51, pp. 46–60, 2019.

[9] R. Naeem, D. Hagerman, J. Alvén, and F. Kahl, "Reftr: Recurrent refinement of confluent trajectories for 3d vascular tree centerlines," *arXiv preprint arXiv:2511.20823*, 2025.

[10] Z. Zhao, Z. Zhang, Y. Liu, Z. Zhang, H. Yu, D. Wang, and L. Wang, "Deformcl: Learning deformable centerline representation for vessel extraction in 3d medical image," in *Proceedings of the IEEE/CVF Conference on Computer Vision and Pattern Recognition (CVPR)*, 2025, pp. 30 896–30 905.

[11] O. Ronneberger, P. Fischer, and T. Brox, "U-net: Convolutional networks for biomedical image segmentation," in *Medical Image Computing and Computer-Assisted Intervention (MICCAI)*, 2015, pp. 234–241.

[12] F. Isensee, P. F. Jaeger, S. A. Kohl, J. Petersen, and K. H. Maier-Hein, "nnu-net: a self-configuring method for deep learning-based biomedical image segmentation," *Nature Methods*, vol. 18, no. 2, pp. 203–211, 2021.

[13] R. Gharleghi, D. Adikari, K. Ellenberger, S.-Y. Ooi, C. Ellis, C.-M. Chen *et al.*, "Automated segmentation of normal and diseased coronary arteries–The ASOCA challenge," *Computerized Medical Imaging and Graphics*, vol. 97, p. 102049, 2022.

[14] C. Prabhakar, B. Wittmann, T. Amiranashvili, P. Büschl, E. de la Rosa, J. McGinnis, B. Wiestler, B. Menze, and S. Shit, "Vesseltok: Tokenizing vessel-like 3d biomedical graph representations for reconstruction and generation," *arXiv preprint arXiv:2603.18797*, 2026.

[15] A. Sinha and G. Hamarneh, "Trind: Representing anatomical trees by denoising diffusion of implicit neural fields," in *Medical Image Computing and Computer Assisted Intervention (MICCAI)*, 2024.

[16] Y. Qi, Y. He, X. Qi, Y. Zhang, and G. Yang, "Dynamic snake convolution based on topological geometric constraints for tubular structure segmentation," in *Proceedings of the IEEE/CVF International Conference on Computer Vision (ICCV)*, 2023, pp. 6070–6079.

[17] Y. Chen, G. Huang, S. Zhang, and J. Dai, "Dynamic snake upsampling operator and boundary-skeleton weighted loss for tubular structure segmentation," *arXiv preprint arXiv:2505.08525*, 2025.

[18] C. D. Murray, "The physiological principle of minimum work. i. the vascular system and the cost of blood volume," *Proceedings of the National Academy of Sciences*, vol. 12, no. 3, pp. 207–214, 1926.

[19] Y. Huo and G. S. Kassab, "Intraspecific scaling laws of vascular trees," *Journal of The Royal Society Interface*, vol. 9, no. 66, pp. 190–200, 2012.

[20] G. Finet, M. Gilard, G. Rioufol, and H. Le Breton, "Fractal geometry of coronary bifurcations: relationship between parent vessel diameter and daughter vessel diameters," *Archives des Maladies du Coeur et des Vaisseaux*, vol. 97, no. 11, pp. 1061–1068, 2004.